Egypt. J. Chem. **Vol. 68**, No. 3. pp. 511 - 524 (2025)

Egyptian Journal of Chemistry

http://ejchem.journals.ekb.eg/

Ferrite Nano-composites Based on Polyaniline as Solid Electrolytes for Electrical Energy Storage Technology: Broadband Dielectric Spectroscopy Investigations

Naglaa H. S. Nasralla*[1], Walaa A .Abd El-Ghany[1], Gehan M. El Komy[1] , Gamal M. Turky[2]

[1] Electron Microscopy and Thin Films Department, Physics Research Institute, National Research Centre, El-Bohoos str., 12622, Dokki, Giza, Egypt.

[2] Department of microwave Physics and Dielectrics, Physics Research Institute, National Research Centre, El-Bohoos str., 12622, Dokki, Giza, Egypt

Abstract

Electrical energy storage is very crucial and is required in our life for every portable electronic device. Ferrite nanoparticles ($NiFe_2O_4$, $Co_{0.5}Ni_{0.5}Fe_2O_4$ and $CoFe_2O_4$) were prepared by simple co-precipitation process, and their nano-composites based on polyaniline ($CoFe_2O_4$/PANI, $Co_{0.5}Ni_{0.5}Fe_2O_4$/ PANI and $NiFe_2O_4$/PAN) assigned as (S1, S2, and S3) respectively were synthesized by the in-situ chemical oxidative polymerization method. The structure of the produced samples was analyzed by X-ray diffraction (XRD), A cubic phase structure of $CoFe_2O_4$ in addition to a tetragonal phase of Fe_2O_3 nanoparticles were identified and they embedded in a semi-crystalline PANI matrix with a higher degree of crystallinity. The crystallite size of 6.98, 5.74, and 6.14 nm were calculated for S1, S2, and S3 respectively. The field emission scanning electron microscope (FESEM) with energy dispersive x-ray mapping analysis was used to analyze the surface morphology. The optical energy gap of the prepared nano-composites was studied by the UV-vis technique. The calculated energy gaps 1.08, 1.0, and 1.04 eV for S1, S2, and S3 respectively were found to slightly change with composition. Magnetic hysteresis loop of nano-composites were recorded at room temperature using a vibrating sample magnetometer (VSM). The magnetic parameters; saturation magnetization Ms, remanenet magnetization M_r, and corecivity have been measure. The highest saturation magnetization (Ms), coerecivity (H_c) and squreness were registered for $CoFe_2O_4$/PANI nanocomposite (13.686 emu/gram, 55.759 Oe and $29.333*10^{-3}$ respectively.) due to the magnetic anisotropy of cobalt. The dielectric properties: permittivity, dielectric loss, and AC conductivity were evaluated in the frequency range from 10^{-1} Hz to 10^7 Hz using a Novo control Alpha analyzer. The $Ni_{0.5}Co_{0.5}Fe_2O_4$/PANI nano-composite sample introduces excellent prospective permittivity, which in turn leads to a significant improvement in capacitance. On the other hand, it showed the highest conductivity. So, the $Ni_{0.5}Co_{0.5}Fe_2O_4$/PANI nano-composite offers great prospects for electrical energy storage applications as well as a promising active electrode material for energy storage appliances and electromagnetic wave filters.

Keywords: Ferrite nano-composites; optical; magnetic; dielectric; energy storage.

1. Introduction

Due to ferrite nanoparticles' appealing electrical, magnetic, and optical properties that indicate their roles in a range of intriguing applications, including drug delivery, high-density information storage devices, microwave devices, and hyperthermia, many studies on the material have been conducted over the past 20 years [1-4]. Nickel ferrites are the most stable, mechanically hard, coercive, and saturation magnetized of all the spinel ferrite nanoparticles [5, 6]. The main reason behind the insertion of ferrite nanoparticles into polymers is their extreme agglomeration, which causes them to coalesce very fast in the absence of a trapping medium or other encapsulating agent [7, 8].

The capping agents improve the surface state and chemical passivation of ferrite nanoparticles, which partially inhibits agglomeration [9]. The optical and electrical performance of ferrite nanoparticles is strongly influenced by reducing agglomeration and maintaining nanoscale particle size [10]. [11]. [12]. Over the last twenty years, ferrite nanocomposites based on polymers have been the subject of various studies. It exhibits complementary behavior with polymer and ferrite nanoparticles [13] and is used in industry for applications such as biosensors, tissue engineering, electrochromic, electromagnetic, corrosion-preventing materials, and electric rechargeable batteries [14]. Integrated circuits, batteries, field-effect transistors, electrical or optoelectronic devices, and other types of sensors are a few other examples [15, 16]. Numerous

*Corresponding author e-mail:nh.nasrallah@nrc.sci.eg; naglaah2001@yahoo.com; (Naglaa Hussain Saleh Nasralla).

Received date 25 June 2024; revised 24 July 2024 ; Accepted date 28 July 2024

DOI: 10.21608/EJCHEM.2024.298829.9901

researchers have examined PANI and its nanocomposites as an effective adsorbent for dye elimination and other organic contaminants from wastewater, and they remain a viable option for environmental applications [17-19]. The production of a composite thin film of tungsten trioxide and polyaniline, as well as the rapid evolution of oxygen electrocatalytic activity, were reported by Alenad et al. [20]. The dielectric and thermal characteristics of PVDF/PVP/$Co_{0.6}Zn_{0.4}Fe_2O_4$ polymer nanocomposite films were studied by Taha et al. [21]. The impact of PVC/PVP/$ZnFe_2O_4$ polymer concentration on the thermal and dielectric properties of the nanocomposites was created by Alshammari et al. [22]. Polyester/$Ni_{0.5}Zn_{0.5}Fe_2O_4$nano-composites were made, and their thermal and dielectric properties were analyzed by T. A. Taha et al. [23]. PmPD/$ZnNiFe_2O_4$nano-composites were created by Kumar et al. [24] using an in-situ chemical oxidative polymerization technique using ammonium persulphate as an oxidant. The dielectric characteristics of the nano-composites were examined at various temperatures and frequencies.

In the current study, nano-composites of $CoFe_2O_4$ /PANI, $Co_{0.5}Ni_{0.5}Fe_2O_4$/ PANI, and $NiFe_2O_4$ /PANI have been prepared by in-situ chemical oxidative polymerization method. The prepared nano-composites were characterized by XRD, FESEM, UV-vis spectrophotometer, VSM and broadband dielectric spectroscopy BDS which is a very important tool to study the electrical and dielectric performance of the prepared samples. It is useful in understanding the structure, the molecular mobility and the mechanism of charge transport in polymers and their nano-composites. However, different techniques can be used to investigate the molecular and sub-molecular mobility of different polymeric systems, like ellipsometry, specific heat spectroscopy and quasi-elastic neutron scattering and BDS allows measurements in a wide range of frequencies and different temperatures as well [25, 26].

2. Results and Discussion

2.1. Structure and Morphology

2.1.1. X-ray diffraction (XRD) analysis

Fig. 1 shows the X-ray diffraction patterns (XRD) of $CoFe_2O_4$/PANI, $Co_{0.5}Ni_{0.5}Fe_2O_4$/ PANI and NiFe2O4/PANI nano-composites assigned as S1, S2, and S3 respectively. The XRD of all samples displays two broad peaks at around 2θ = 20.35° and 25.3 corresponds to PANI [30-33]. The XRD patterns of $CoFe_2O_4$/PANI, $NiCoFe_2O_4$/PANI and $NiFe_2O_4$/PANI demonstrate peaks at 2θ = 35.51° and 53.89° corresponding to (311) and (422) planes, respectively for ferrite composites either cubic CoFe2O4 (JCPDS Card No. 03-0864) or cubic Ni0.4Fe2.6O4 (JCPDS Card No. 87-2335). Furthermore, there are peaks at 2θ = 24.08°, 33.05°, 40.74°, 49.30°, 62.25°, and 63.78° corresponding to (012), (104), (113), (024), (214), and (300) planes, respectively which belong to rhombohedra Fe2O3 (JCPDS Card No. 24-0072) and a peak at 71.71° corresponding to (206) plane that belong to tetragonal Fe2O3 (JCPDS Card No. 65-0390). Among the various composites, CoFe2O4/PANI has been observed to exhibit a higher degree of crystallinity. This may be due to the uniform distribution of $CoFe_2O_4$ in the PANI chain and their interaction with each other forming complex particles that are responsible for crystallinity [34, 35]. This can be confirmed by calculating the crystallinity percentage, which is given by [36, 37]:

$$C\% = A_s/A \quad (1)$$

C%: percent crystallinity, As: the total area of crystalline peaks, and A: the total area of all peaks.

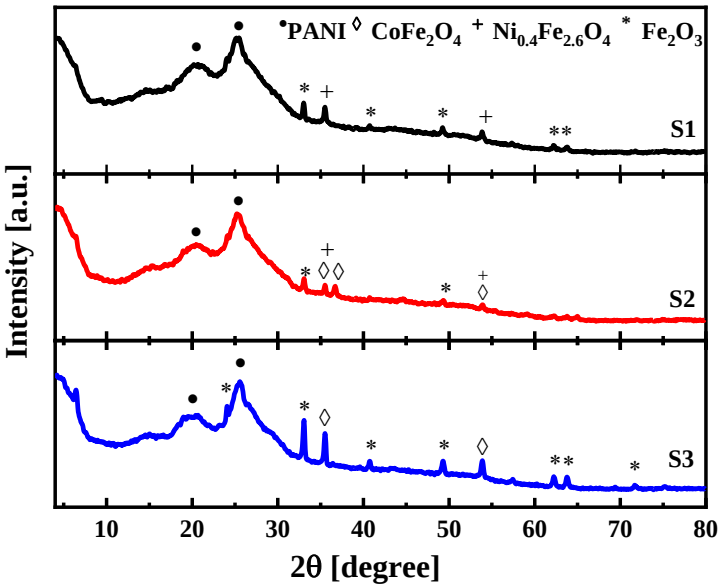

Figure 1: X-ray diffraction patterns of $CoFe_2O_4$/PANI, $Co_{0.5}Ni_{0.5}Fe_2O_4$/ PANI and $NiFe_2O_4$/PANI nano-composites assigned for S1, S2, and S3 respectively.

The calculated values of the crystallinity percentage for different composites are recorded in Table 1. The crystallite size (*D*) of each composite can be calculated by using Scherer's equation, which states that the full width at half maximum (β) of the main peak is related to the wavelength (λ) and the angle (θ) of the incident x-ray radiation by:

$$D = \frac{0.9\lambda}{\beta\cos\theta} \qquad (2)$$

The crystallite sizes for different samples are listed in Table 1. It is observed that the $CoFe_2O_4$/PANI nanocompositehad the greatest crystallite size D. This is due to the difference in ionic radius, where the radius of Co (125 pm) compared to Ni (124 pm) [33]. Moreover, the dislocation density (δ) can be calculated by the following equations [34, 35]:

$$\delta = \frac{1}{D^2} \qquad (3)$$

Table 1 shows the calculated values of δ for the prepared nano-composites. Following the table, the nanocomposite $CoFe_2O_4$/ PANI has the lowest dislocation density, indicating the highest level of crystallinity[38].

Table 1: The crystallinity%, the crystallite size (D), and the dislocation density of the prepared nano-composites.

Sample	Crystallinity %	D (nm)	$\delta\times 10^2$ (nm^{-2})
$CoFe_2O_4$/PANI	61.17	6.98	2.05
$Co_{0.5}Ni_{0.5}Fe_2O_4$/ PANI	55.34	5.74	3.03
$NiFe_2O_4$/PANI	56.45	6.14	2.66

2.1.2. Morphological Analysis

The morphologies of synthesized PANI, $CoFe_2O_4$/PANI, $Co_{0.5}Ni_{0.5}Fe_2O_4$/ PANI and $NiFe_2O_4$/PANI nano-composite were investigated by FESEM and Energy dispersive x-ray mapping techniques. Figure 2 illustrates the morphology of pure polyaniline with a fibrous structure formed initially due to the linear chain of polyaniline, as seen from the inset of the figure with higher magnification. The polyanilinenanofibers tend to agglomerate and form micro-size particles,whereas the $CoFe_2O_4$/PANI nanocomposite morphology revealed spherical nanoparticles of cobalt in the size range of 32 nm to 76 nm with uniform distribution and well dispersion decorating the irregular flakes-like structure of PANI. The morphology of $NiFe_2O_4$-PANI nanocomposites is shown in Fig.3. The polyaniline covered nickel ferrite where nickel ferrite nanoparticles are present during the aniline polymerization process. As a result, during polymerization, nickel ferrite served as an active nucleation point for the polyaniline nanostructures that blanket their surface. Thus, it can be said that the polymer covered the ferrite surface and formed on top of the NF surface. On average, the grain size ranged from around 35 nm to 78.5 nm. The morphology of $NiFe_2O_4$/PANI and $NiCoFe_2O_4$-PANI nanocomposites (Fig 3) reveals that the surface morphology has mostly changed to disordered agglomerates after the incorporation of both cobalt and nickel ferrite into polyaniline, and the particle size is about 36 nm to 60 nm. The elemental components in nanocomposites Co, Ni, and CoNi ferrite/PANIcan be investigated through FESEM-mapping as clearly shown in Figs 2 and 3. The presence of C, N, O, Fe, Co, and Ni distributions is confirmed. A tiny percentage of S is due to the APS ions left behind after the process.

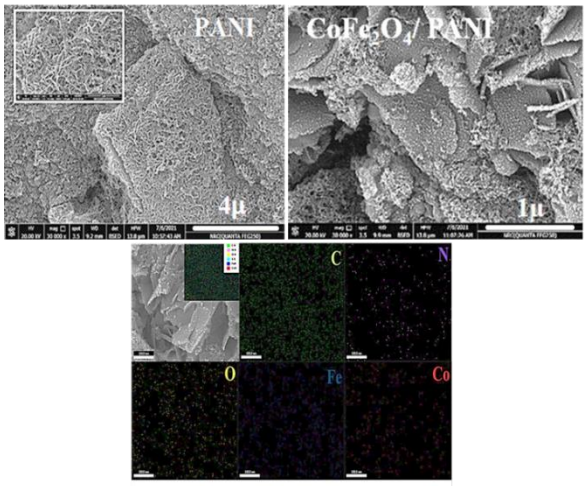

Figure 2: The morphology and Energy dispersive X-ray mapping of pure PANI and $CoFe_2O_4$ /PANI nano-composites.

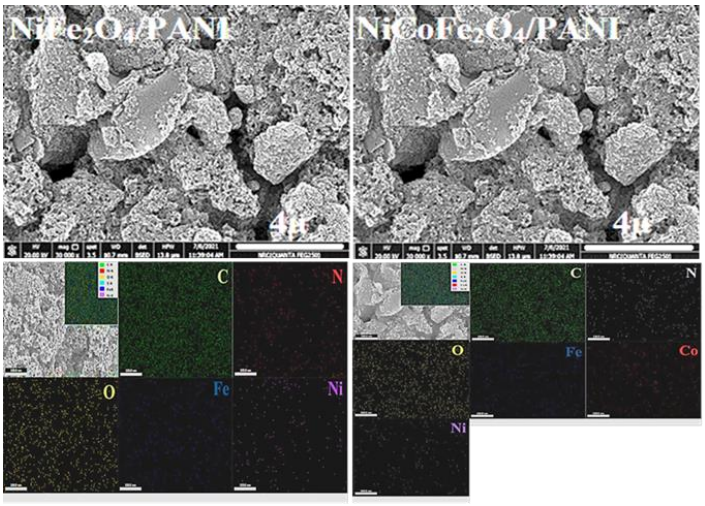

Figure 3: The morphology and the Energy dispersive X-ray mapping of Ni Fe_2O_4/PANI and $Co_{0.5}Ni_{0.5}Fe_2O_4$/ PANI nanocomposites.

2.2. Optical properties

The optical properties of $CoFe_2O_4$/PANI, $Co_{0.5}Ni_{0.5}Fe_2O_4$/ PANI and $NiFe_2O_4$/PANI nano composites can be studied by applying the Kubelka–Munk (K–M) method based on the following equation [33, 39]:

$$F(R) = \frac{(1-R)^2}{2R} \qquad (4)$$

Where *R* is the diffuse-reflectance; *F(R)* is proportional to the absorption coefficient *(α)*.This equation is typically used for highly light-scattering materials and absorbing particles within a matrix. Fig. 4 illustrates the dependence of diffuse reflectance on the wavelength for all samples. The plot shows a small peak at 368 nm attributed to π —π^* transition in the benzenoid rings of polyaniline[40, 41]. Additionally, there is an absorption band at 434–488nm and a peak at 856 nm corresponding to polaron— π^* band and π — polaron band transitions, respectively [42, 43].

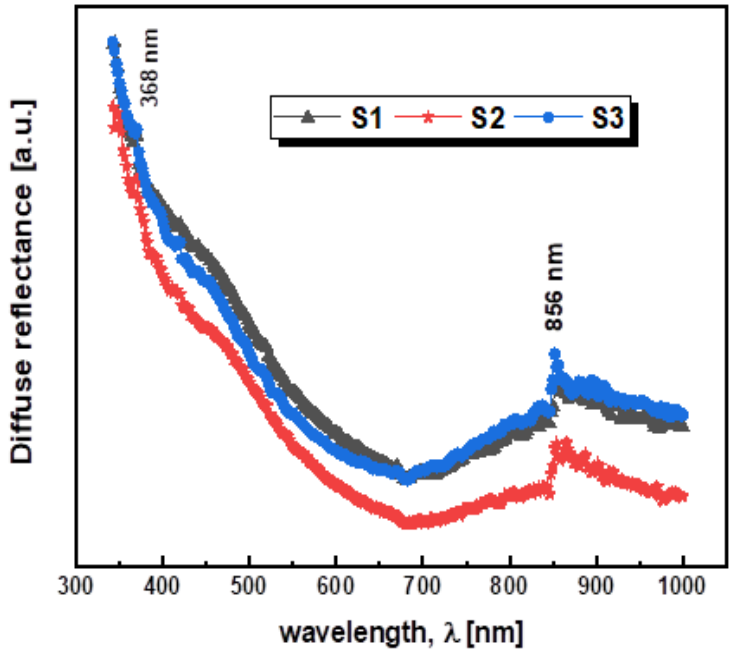

Figure 4: Dependence of diffuse reflectance on the wavelength for $CoFe_2O_4$-PANI, $Co_{0.5}Ni_{0.5}Fe_2O_4$/ PANI and $NiFe_2O_4$/PANI nano-composites assigned as S1, S2, and S3 respectively.

The Tauc relation has been applied when determining the optical band gap of the prepared samples. which is given by [44]:

$$\alpha = \frac{A(E - E_g)^n}{h\nu} \qquad (5)$$

Where *A* is constant depending on the transition probability, E_g,is the optical band gap, and $h\upsilon$ is photon energy. The values of n are 2, 1/2, 3, or 3/2, corresponding to transitions that are indirect allowed, direct allowed, indirect forbidden and direct forbidden transitions, respectively. When n = 1/2, the prepared samples fit together the best, suggesting a direct permitted transition.

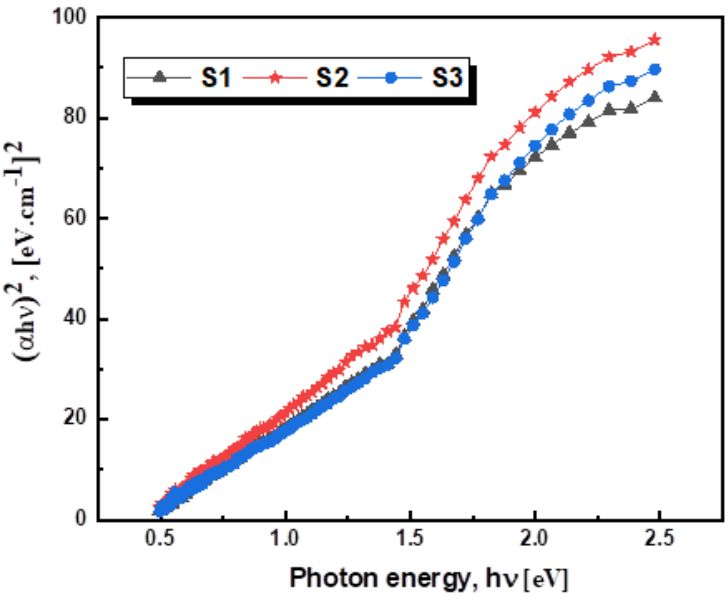

Figure 5: The plots of $(\alpha h\nu)^2$ as a function of hν for for $CoFe_2O_4$-PANI, $Co_{0.5}Ni_{0.5}Fe_2O_4$/ PANI and $NiFe_2O_4$/PANI nano-composites are assigned as S1, S2, and S3 respectively.

Figure 5 represents a plot of $(\alpha h\upsilon)^2$ versus photon energy, hυ. The linear portion has been extrapolated to hν, where α = 0, to estimate the optical band gap, E_g. The values of E_g are 1.08 eV, 1.00 eV, and 1.04 eV for S1, S2, and S3 respectively. The optical band gap of $NiCoFe_2O_4$/ PANI is smaller than the others and comparable to other related works, as seen in Table 2.

Table 2; The optical band gap E_g of current nanocomposites and related nanocomposite.

Nanocomposites	**E_g**	
Co Fe_2O_4/PANI	1.08	**Current work**
$Co_{0.5}$ $Ni_{0.5}$ Fe_2O_4/PANI	1.00	
Ni Fe_2O_4 /PANI	1.04	
Co–Zr doped Ni ferrite/PANI	2.0	Ref [45]

2.3. Magnetic characterization

A vibrating sample magnetometer (VSM) was used to measure the magnetic properties of the materials under investigation. To measure it briefly, a positive magnetic field H was supplied to the synthesized samples. Subsequently, the sample underwent vertical vibration, generating an induced magnetic field that matched the sample's magnetization in terms of induced current. The magnetic field was reduced to zero once the sample's magnetization reached Ms, although some magnetization persisted in the ferromagnetic sample. Therefore, the coercive field Hc is a negative magnetic field that was used to eliminate the residual magnetization, which is called the coercive field H_c. The M-H hysteresis loops were obtained by repeating this cycle. The magnetic properties of ferrite powders Co Fe_2O_4/PANI, $Co_{0.5}$ $Ni_{0.5}$ Fe_2O_4/PANI and Ni Fe_2O_4/PANI were measured by VSM under the effect of applied magnetic field ranging from −20 to 20 kOe at room temperature. The

magnetic hysteresis loops of the prepared spinel ferrites and their zoom range are shown in Fig. 6a, b. revealing soft ferromagnetic behavior. The ferrimagnetism observed in the investigated samples results from anti-parallel spins between Fe^{3+} and Ni^{2+}/Co^{2+} at different sites. It was demonstrated that the cation distribution in the majority of nano-size spinel ferrites had an intermediate degree of inversion, with both sites containing a portion of the divalent and trivalent cations, or mixed spinels.

Nickel ferrite's microstructural and magnetic characteristics can be efficiently tuned and controlled by partially substituting Co^{2+} for Ni^{2+}. $CoFe_2O_4$/ PANI sample indicated a higher magnetic saturation (M_s) of 13.686 emu/g in comparison with Co Ni Fe_2O_4/ PANI (11.733 emu/g) and Ni Fe_2O_4/ PANI (7.90 emu/g). On the other hand, the lowest coercive field H_c observed for $NiFe_2O_4$/ PANI can be due to the smaller grain structure. The magnetic element Co caused a higher magnetization for $CoFe_2O_4$/ PANI and Co Ni Fe_2O_4/ PANI compared to Ni Fe_2O_4/ PANI. Table 3 presents the values of coercivity (Hc), remanent magnetization (Mr), and saturation magnetization (Ms) derived from hysteresis loops. The detected values of saturation magnetization, retentivity, and coercivity verified the presence of soft magnetic Ni-Co phase and Co phase [46]. Increasing the values of squareness with composition variation proved that the Co phase with Fe_2O_3 is suitable and desired for the recording medium devices application.

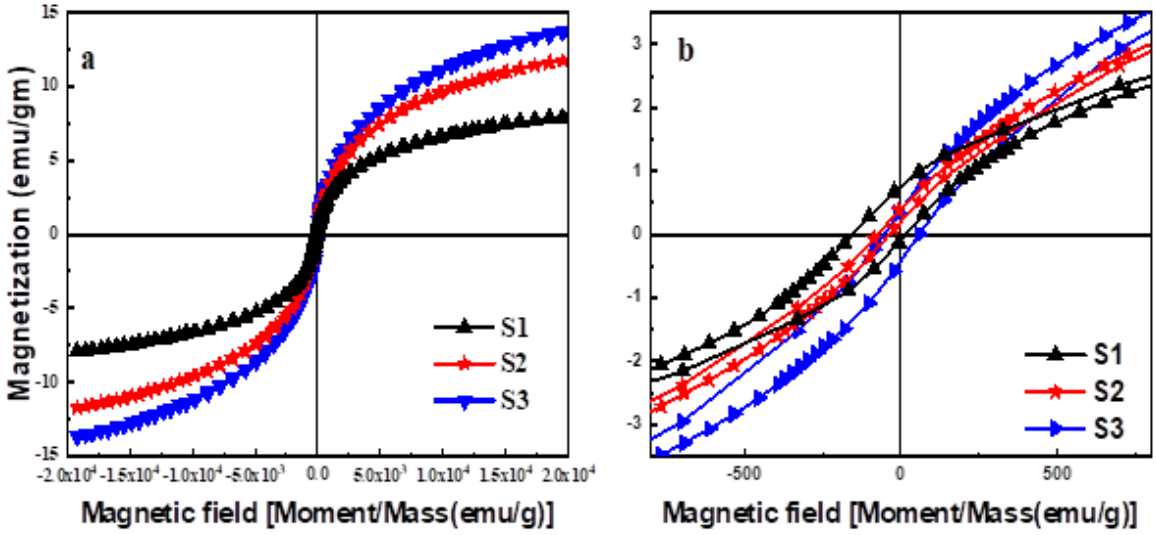

Figure 6 a - b (a): Magnetic hysteresis curves of Co Fe_2O_4/PANI, Co $_{0.5}Ni_{0.5}$ Fe_2O_4/PANI and Ni Fe_2O_4 /PANI in the magnetic range from -2000 Oe to 2000 Oe , (b) Zoom to (MH) in from -900 to 900 Oe.

Table 3: The magnetic parameters extracted from the hysteresis curves ; The saturation magnetization M_s, the remanant magnetization M_r, exchange bias $H_{ci}$and squarness SQR; 1, 2 and 3 are the current composites where 4, 5 and 6 other related composites.

	Nanocomposites	Ms (emu/gram)	Mr (emu/gra)	Hc Coercivity(Oe)	SQR	
						Current work
1.	$CoFe_2O_4$/PANI	13.686	0.40146	55.759	$29.333*10^{-3}$	
2.	$Co_{0.5}Ni_{0.5}Fe_2O_4$/PAI	11.733	0.14517	25.702	$12.374*10^{-3}$	
3.	$NiFe_2O_4$ /PANI	7.9025	$67.830*10^{-3}$	11.954	$8.583*10^{-3}$	
4.	$NiFe_2O_4$/50%PANI	13.36	8.59	307	-----	Ref [47]
5.	$NiFe_2O_4$/25%PANI	6.24	3.95	303	-----	Ref [47]
6.	PANI/CoFe2O4	17.5	-------	------	-----	Ref [48]

When the dimensions are only a few nanometers, a ferromagnet, like iron, has a large exchange parameter but a comparatively tiny anisotropy. Large anisotropies and correspondingly stable orientations are seen in several antiferromagnets, such as NiO. Exchange coupling between ferromagnets and antiferromagnets in heterostructures can theoretically result in ferromagnetic behavior with high anisotropy and stable order [49].

2.4. Dielectric study

The dielectric spectroscopy is very important tool for studying the electrical and dielectric performance of $CoFe_2O_4$-PANI, $CoNiFe_2O_4$-PANI, and $NiFe_2O_4$-PANI nano-composites which are assigned as S1, S2, and S3 respectively. Therefore, the dielectric parameters: permittivity, ε', dielectric loss, ε", as the real and imaginary parts of the complex permittivity, ε*, in addition to the electric loss modulus (M"), dissipation factor, tan δ, and AC conductivity (σ_{ac}) have been measured over a wide frequency range ranging from 10^{-1} to 10^7 Hz at room temperature. These dielectric and electrical parameters are interrelated according to [50]:

$$\varepsilon^*(\omega) = \varepsilon'(\omega) - i\varepsilon''(\omega) = \frac{1}{M^*} = \frac{\sigma^*}{i\omega\varepsilon_o} \quad (6)$$

Implying that:

$$\sigma' = \varepsilon_0 \omega \varepsilon'' \quad (7)$$

And

$$M'' = \frac{\varepsilon''}{\varepsilon'^2 + \varepsilon''^2} \quad (8)$$

$$\tan\delta = \frac{\varepsilon''}{\varepsilon'} \quad (9)$$

Where ε_o is the free-space permittivity, ω is the radial frequency = 2πν (ν is the frequency), ε' and ε" are the real and imaginary parts of the dielectric permittivity, respectively. The samples were prepared between two gold-plated stainless-steel electrodes in a parallel plate capacitor configuration. A material's capacity to store electric energy in the form of polarization is indicated by its permittivity, also known as its dielectric constant (ε'). The maximum permittivity of energy storage devices is necessary to improve their electrical performance.

Fig.7 displays the frequency dependence of the permittivity, ε', with the three different compositions under investigation. There are three distinguished trends that could be seen here. The permittivity increases rapidly with decreasing frequency, starting from 100 kHz down to 0.1 Hz. This originates basically from the superposition of the well-known electrode polarization (which results from the charge carriers building up at the electrode/composite interface) and the contribution of charge carrier transport (which causes conductivity). For all samples, the abrupt increase in ε' as the frequency decreases in this range is clear with the highest permittivity for S2. The intermediate frequency window (10^2 – 10^5 Hz) shows a dispersion step-like behavior attributed to interfacial polarization, which is usually found in such heterogeneous structures. A further increase of the frequency than 10^5 Hz, shows more or less stability of the permittivity values. In other words, the effect of the frequency on the permittivity is reduced remarkably. This clearly reflected the lag of the fluctuations for all kinds of polarizations behind the frequency of the external applied field in such high-frequency range. The composition of the considered sample plays the main role of the permittivity values and not the frequency.

The prevalence of interfacial or Maxwell-Wagner-Sillars (MWS) polarization [51] is caused by the conductivity difference between the composite polymer matrix and the dopants, which causes free charges to accumulate at the Co, Ni, and PANI interfaces. According to this model, grains and grain boundaries should be present in the dielectric structure. The grain boundaries are active in low-frequency regimes offering high resistance and thus giving high permittivity values; instead, in high-frequency regime, electric dipoles are responsible for the materials' dielectric relaxation at lower frequencies.

The large value of the real part of the dielectric constant at lower frequencies is attributed to these dipoles because they have enough time to respond to the applied frequency. Higher frequencies, on the other hand, cause the dipoles to be unable to reorient in response to the applied oscillating fields, leading to a delayed reaction and lower dielectric constant values. Where the effect of grains is dominating producing almost linear permittivity. Additionally, at higher frequencies starting from 10^5 Hz, less effect could be noticed here, either due to frequency or composition, on the determined values of permittivity as it appears almost constant and has collapsed in one decade over this frequency window. This can be explained according to the fact that at higher frequencies any fluctuations of polarizations or hopping mechanisms of charge carries lag behind the frequency of the external applied electric field. The highest permittivity value ε' was observed for the S2 ($Co_{0.5}$ $Ni_{0.5}$ Fe_2O_4) / PANI) sample, which could be confirmed from XRD results, where it has the smallest grain size (5.74 nm), the highest dislocation and the less crystallinity compared to S1 and S3. The coexistence of both Co and Ni in the Nano composite results in the formation of polarization states due to space charge accumulating at the interfaces, as previously discussed in the FESEM study, leading to high dielectric permittivity.

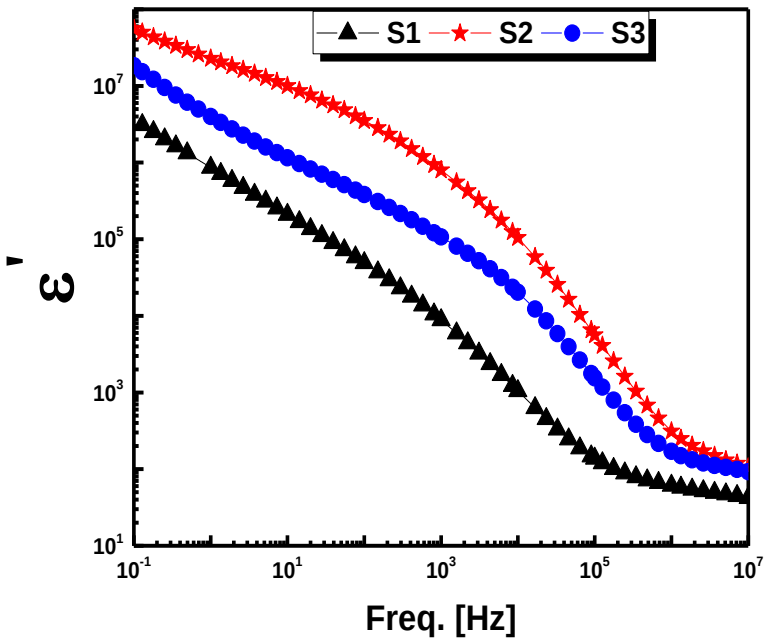

Figure 7: The frequency dependence of permittivity (ε') of $CoFe_2O_4$-PANI, $Co_{0.5}Ni_{0.5}Fe_2O_4$-PANI and $NiFe_2O_4$-PANI nano-composites are assigned as S1, S2, and S3 respectively.

The second attribute required for evaluating a material's electric performance is its ac-conductivity, or σ′ (ω), which measures the material's electrical conductivity. The DC conductivity, or frequency-independent conductivity, is represented by σ_{dc} under an alternating electric field. Given that σ_{ac} (ω) is dependent on electron hopping, charge carrier mobility, and space charge distribution, it results from free charge carriers moving in the direction of the electric field. Conversely, σ_{dc} results from the erratic movements of free charge carriers, which have significantly smaller values than σ_{ac}.

As seen in Fig. 8, conductivity (σ'_{ac}) has been studied over a broad frequency range. Every sample showed a growing σ'_{ac} trend at two distinct rates in response to the frequency increase. It exhibits a semi-plateau-like characteristic at $f > 10^5$ Hz and grows with frequency at a very sluggish rate. The contribution of frequency-independent conductivity could be responsible for this kind of behavior. On the other hand, σ_{ac} (ω) increases significantly at $f < 10^5$ Hz showing the frequency-dependent conductivity. This behavior is due to electrode polarization, as confirmed by the peak appearing at the imaginary part of the conductivity (σ''_{ac}) plot as shown in the lower inset of Fig. 8.

In addition, an increase in σ_{ac} observed at low frequency can be explained by a rise in the mobility or concentration of free charge carriers, which in turn causes an increase in σ_{ac}. The existence of some relaxation peaks revealed the presence of relaxation phenomena inside these composites.

For all samples, the conductivity at a given frequency of 10^5 Hz was examined as a representative study behavior due to the composition effect, as shown in the upper inset of Fig. 8. As was previously mentioned in the permittivity section, the coexistence of more interfacial layers is responsible for the increase in the value of S2's ac conductivity. It is worth mentioning that an expected competition between different parameters affects the conductivity behavior as the effect of NH^{+4} in decreasing the charge carriers through capturing H^+ by NH^{+3} in the PANI framework leads to decreasing the conductivity.

On the other hand, the opposite behavior is observed by incorporation of Ni Co Fe_2O_4 into the PANI matrix as increase in conductivity and more predominant than the previous effect. The noticeable shift in frequency and conductivity (σ' and σ") due to the composition change is attributed to the effect of incorporation of insulating material into the conductive one.

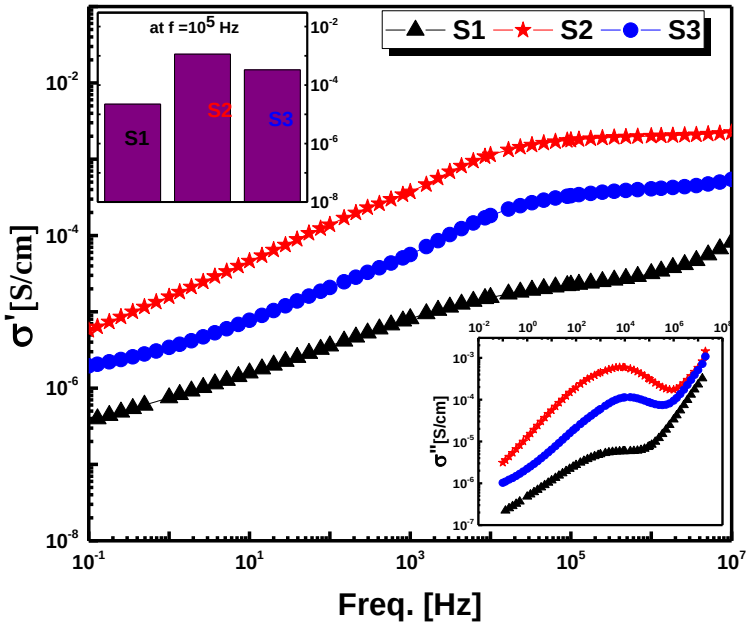

Figure 8: The frequency dependence of the real part of AC conductivity (σ') of $CoFe_2O_4$-PANI (S1), $Co_{0.5}Ni_{0.5}Fe_2O_4$-PANI (S2) and $NiFe_2O_4$-PANI (S3) nano-composite.

The frequency dependence of dielectric loss (ε") and modulus (M") has been studied. They represent the electrical energy lost by the material as heat or/and leakage current, as shown in Figs. 9 and 10 respectively. The variation of ε" with frequency for all composites which includes the effects of both molecular dynamics and conductivity, sharply decreases with increasing frequency and composition. The highest value was observed for S2 sample with a hump-like peak at intermediate frequency range which is an indication for the electrode polarization as the free charges are blocked at sample/electrode interfaces which clearly observed as a steep increase in the dielectric constant (ε'). The highest energy loss is related to the high dielectric loss that is obtained at lower frequencies because of active resistive grain boundaries and the increased energy needed for electron hopping between Fe^{2+} and Fe^{3+} ions. Because conducting grains are active at higher frequencies, less dielectric loss occurs and less energy is needed for the electron hopping process [24].
The electrical response can be analyzed by the complex electric modulus (M*) to investigate the dielectric relaxation processes of the composites.

The evolution of the imaginary part (M") of the modulus as a function of frequency at room temperature is shown in Fig. 10. The imaginary part of the modulus (M") exhibits an increase by increasing the frequency for S2 showing the least value of M'' and a higher value for ε'. The relaxation peak starts to be noticed at a higher frequency at different positions for each sample but is not completely seen, it may be it is out of the frequency range. This variation in the peak position of the imaginary part of the modulus of the composite could be related to the difference in the microstructure. All the previous parameters decrease the relaxation time and confirm that the relaxation is frequency and composition dependent.
It is known that the phenomenon of polarization is the result of an applied ac field that leads to the storage of energy in a material. Under the recovery of this energy, some of its amount is dissipated in the form of heat, which is quantitatively measured in the form of loss tangent (Tanδ). Fig.11 depicts the variation of Tan δ versus log f for all samples. The occurrence of relaxation peaks in the observation of tanδ is due to the equalization of the applied ac field and localized mobility carrier's frequencies, which is comparable to that of Rezlescu's model [52]. Furthermore, these relaxation peaks represent the presence of some structural defects in the samples. Moreover, S2 sample shows the highest value of tan δ relaxation peak appeared at higher frequency which affirmed the optimized response of this composition.

Based on all of the earlier findings, it can be said that many mechanisms contribute to the ε′ when electromagnetic (EM) waves pass over the nanocomposites samples. Interfacial polarization is the first effect of free charges building up at the edges of composite surfaces during composite synthesis because of differences in conductivity. Second, dipolar polarization will be facilitated by the dipoles found in the PANI as well as the dipoles created by the ions (Ni^{2+}, Co^{2+}, Fe^{2+}, Fe^{3+} and O^{2-}) in $NiCoFe_2O_4$[53]. When Ni and Co coexist, there may be greater electric energy storage, which is directly linked to an increase in the S2 nanocomposite's capacitance and ε′.
Furthermore, the losses ε″ resulting from Debye relaxation in the nano-composite matrix may also be influenced by the interfacial polarization and dipolar polarization phenomena.

As all dielectric parameters are sensitive to material changes brought about by processes like the addition of fillers, composition changes, and so on. Moreover, addition of insulating $NiCoFe_2O_4$ to the conductive PANI decreases or breaks the conductive gride of PANI partially so the EM waves could be transmitted to the composite interiors effectively, which means loss of incident EM waves. This could be utilized to be used as EM filters [53].

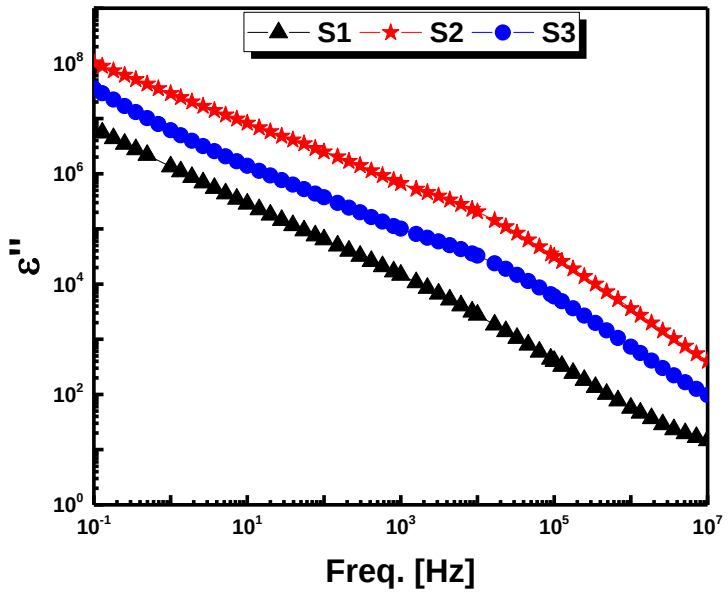

Figure 9: The frequency dependence of dielectric loss (ε") of $CoFe_2O_4$-PANI, $Co_{0.5}Ni_{0.5}Fe_2O_4$-PANI and $NiFe_2O_4$-PANI nano-composite which are assigned as S1, S2, and S3 respectively

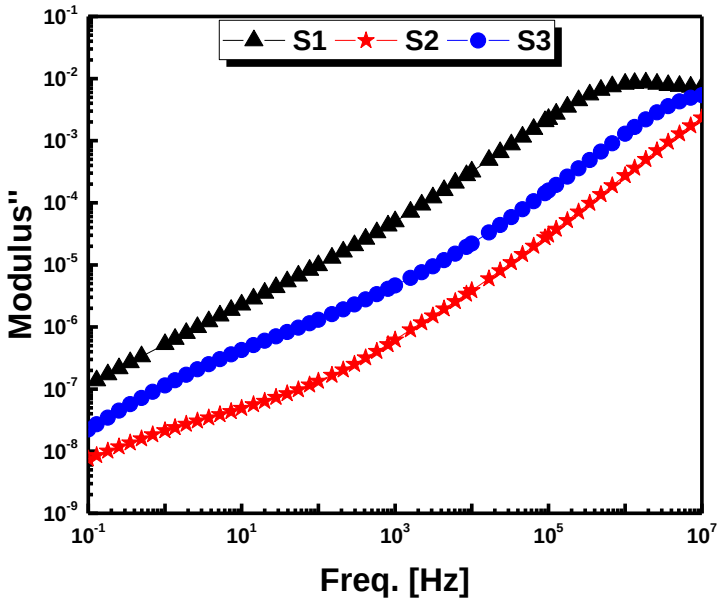

Figure 10. The frequency dependence of the imaginary part (M") of the modulus of $CoFe_2O_4$-PANI, $Co_{0.5}Ni_{0.5}Fe_2O_4$-PANI and $NiFe_2O_4$-PANI nano-composite which are designated as S1, S2, and S3 respectively.

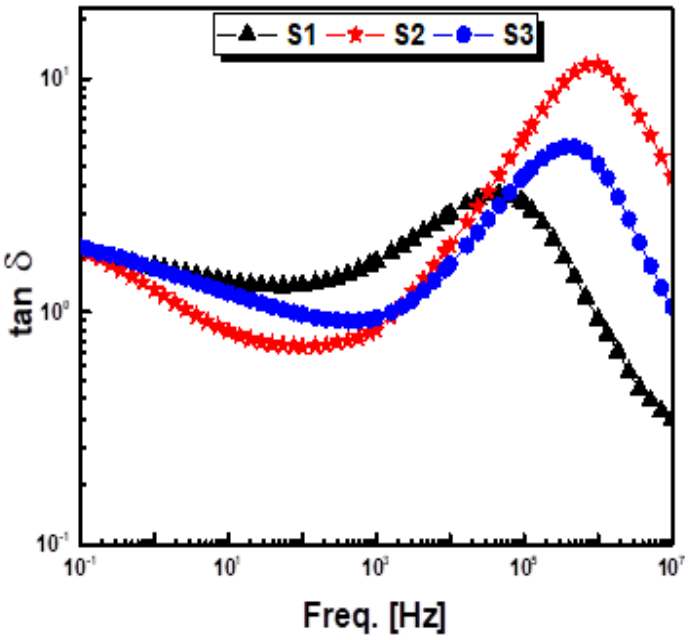

Figure 11. The frequency dependence of the variation of loss tangent (Tan δ) of $CoFe_2O_4$-PANI, $Co_{0.5}Ni_{0.5}Fe_2O_4$-PANI and $NiFe_2O_4$-PANI nano-composite which are assigned as S1, S2, and S3 respectively.

3. Experimental

3.1. Preparation of Ferrite nanoparticles nanoparticles.

Using pure AR grade Merck chemicals (99% pure), a straightforward co-precipitation process were used to prepare the nanoparticles composites of $CoFe_2O_4$, $Co_{0.5}Ni_{0.5}$ Fe_2O_4 and $NiFe_2O_4$ without need for additional purification. For the synthesis of nanoparticles, the $CoSO_4.7H_2O$, $NiSO_4.6H_2O$ and Fe $(NO_3)_3.9H2O$ salts were taken as precursors. The desired stoichiometric properties of metal sulfates and nitrates were weighed. They were dissolved separately in each minimum amount of 20 ml of deionized water. After the whole dissolution, the metal nitrates were mixed to maintain the Ni + Co / Fe ratio of 1:2. The solution was kept with constant stirring at 650 rpm at 80◦C. A precipitating agent, sodium hydroxide (KOH), was added with a pH value around 9. Further, the stirred solution was kept in for 3 hours at 80◦C. Finally, dark brown precipitate was obtained. Deionized water was used for washing the precipitate many times systematically. Additionally, the precipitate was dried in hot air oven for 2 hours at 75 °C to form the synthesized nano-composites and then calcined at 900 °C.

3.2. Preparation of nano-composites based on polyaniline.

To prepare $CoFe_2O_4$ /PANI, $Co_{0.5}Ni_{0.5}Fe_2O_4$/ PANI, and $NiFe_2O_4$ /PANI nano-composites, the in situ polymerization was employed. A solution of 300 mL containing 0.25M aniline in 0.25M HCl was mixed with 0.907 gm. (13 wt% of aniline) from each ferrite. Next, while stirring at 25°C for 12 hours, 300 ml of a solution containing 0.3125 M ammonium persulfate was added in drops to the acidic aniline solution. After separating the polyanilinenano-composite on filter paper and washing it in acetone and deionized water, it was dried in an electrical oven at 90°C. S1, S2 and S3 are the codes of nano-composites samples with 13 wt. % of nickel ferrite, cobalt-nickel ferrites, and nickel ferrite in the polyaniline, respectively.

3.3. Characterization of prepared compounds

Powder X-ray diffraction was used to investigate the crystal structure data based on a Type Diano PW 1370 X-ray diffractometer operating at 35 kV and 100 mA in the 2θ range of 10° - 80° with a fixed Cu Kα radiation (λ = 1.5406 Å). The diffraction patterns were recorded at a scanning rate of 2°/min.

The diffraction patterns were automatically recorded with a scanning rate of 2°/min. The field emission scanning electron microscope (FESEM) model Quanta FEG 250, operating at 35 kV, was used to analyze the film topography and Energy dispersive X-ray mapping. The optical measurements were examined by UV–vis spectrophotometer of type JASCO 570. The magnetic measurements were analyzed at room temperature using a vibrating sample magnetometer (VSM; Lake Shore - 7410-USA). A Novocontrol high-resolution alpha analyzer (Concept 40) was used to examine the electrical conductivity and dielectric characteristics of the investigated samples on frequency range of 0.1 Hz to 20 MHz. The current measurements were carried out at room temperature with an accuracy better than 99%. The samples were prepared in a parallel plate capacitor design of two gold-plated stainless-steel electrodes. More information about the used setup can be found elsewhere [27-29].

4. Conclusions

Simple co-precipitation is used to synthesize ferrite nanoparticles and in-situ polymerization was used to create their polyaniline-based nano-composites. The cubic phase structure of the nanoparticles in the PANI matrix was verified by XRD with the highest degree of crystallinity, lowest dislocation density, and greatest crystallite size with 6.98 nm for $CoFe_2O_4$ /PANI in comparison to PANI /$NiFe_2O_4$ and $Ni_{0.5}Co_{0.5}Fe_2O_4$ /PANI nano-composites. The FESEM and x-ray mapping showed the formation of nanoparticles and homogenous distribution of the constituent elements in the prepared nano-composites. The optical band gap was calculated showing the smaller energy gap (1.0 eV) for $Ni_{0.5}Co_{0.5}Fe_2O_4$ /PANI nanoparticles compared to 1.08 and 1.04 eV for $CoFe_2O_4$ /PANI and NiFe2O4 /PANI nanoparticles respectively. All samples showed soft ferromagnetic behavior at room temperature and an increase in all magnetic parameters depending on the type of composition in the nano-composite. The highest saturation magnetization Ms (13.686 emu/gram), coerecivity (55.759 Oe) and squreness (29.333*10-3) were registered for CoFe2O4/PANI nanocomposite. The dielectric properties of synthesized nano-composites revealed an enhancement of the permittivity, from 106 to 108. According to HafizaVaneezaHussaina et al. [54] as their results of permittivity are in the range of 103 to 106, that means a significant improvement in capacitance with the highest conductivity for $Ni_{0.5}Co_{0.5}Fe_2O_4$ /PANI nano-composites with value (1.14*10-2 S/cm) in comparison to the $CoFe_2O_4$ /PANI (2.23*10-5 S/cm) and $NiFe_2O_4$ /PANI (3.32*10-4 S/cm). According to all the discussed results, the future trend for such nanocomposite ($CoFe_2O_4$ /PANI) is its use in broad application fields, e.g. the recording medium devices electrical energy storage technology as well as in electromagnetic wave filters. Further work should be done using different compositions of the considered nanocomposites in order to optimize the efficiency for such application fields.

5. Conflicts of interest

There are no conflicts to declare.

6. Formatting of funding sources

There are no funding sources.

7. Acknowledgments

We gratefully thank Prof. Mohammed Selim, professor in surface chemistry at National Research Center, for the time and effort provided throughout the year. His useful advice and suggestions were really helpful.

8. References and Bibliography

1. Castro, T., et al., Structural and magnetic properties of ZnO–CoFe2O4 nanocomposites. Journal of Magnetism and Magnetic Materials, 2015. 389: p. 27-33.
2. Hazra, S., et al., A novel ‘one-pot’synthetic method for preparation of (Ni0. 65Zn0. 35Fe2O4) x–(BaFe12O19) 1− x nanocomposites and study of their microwave absorption and magnetic properties. Powder technology, 2015. 279: p. 10-17.
3. Pedroza, R., et al., Raman study of nanoparticle-template interaction in a CoFe2O4/SiO2-based nanocomposite prepared by sol–gel method. Journal of magnetism and magnetic materials, 2005. 289: p. 139-141.
4. Singh, H. and K. Yadav, Synthesis and study of structural, dielectric, magnetic and magnetoelectric characterization of BiFeO3–NiFe2O4 nanocomposites prepared by chemical solution method. Journal of alloys and compounds, 2014. 585: p. 805-810.
5. Sarangi, P.P., et al., Synthesis and characterization of pure single phase Ni–Zn ferrite nanopowders by oxalate based precursor method. Powder Technology, 2010. 203(2): p. 348-353.
6. Sivakumar, M., et al., A new ultrasonic cavitation approach for the synthesis of zinc ferrite nanocrystals. Current Applied Physics, 2006. 6(3): p. 591-593.
7. Badr, Y., K. Abd El-Kader, and R.M. Khafagy, Raman spectroscopic study of CdS, PVA composite films. Journal of applied polymer science, 2004. 92(3): p. 1984-1992.
8. Liangchao, L., et al., Preparation and magnetic properties of Cu0. 4Zn0. 6Cr0. 5Sm0. 06Fe1.44O4/polyanilinenanocomposites.Journal of Rare Earths, 2008. 26(4): p. 558-562.
9. Ikenaga, N.-o., et al., Preparation of zinc ferrite in the presence of carbon material and its application to hot-gas cleaning. Fuel, 2004. 83(6): p. 661-669.
10. Javed, R., et al., Role of capping agents in the application of nanoparticles in biomedicine and environmental remediation: recent trends and future prospects. Journal of Nanobiotechnology, 2020. 18: p. 1-15.
11. Kyrychenko, A., D.A. Pasko, and O.N. Kalugin, Poly (vinyl alcohol) as a water protecting agent for silver nanoparticles: The role of polymer size and structure. Physical Chemistry Chemical Physics, 2017. 19(13): p. 8742-8756.
12. Alhassan, S., et al., Preparation and Optical Properties of PVDF-CaFe2O4 Polymer Nanocomposite Films. Polymers, 2023. 15(9): p. 2232.
13. Fu, S., et al., Some basic aspects of polymer nanocomposites: A critical review. Nano Materials Science, 2019. 1(1): p. 2-30.
14. El-Sayed, N.S., et al., Synthesis and characterization of polyaniline/tosylcellulose stearate composites as promising semiconducting materials. Synthetic Metals, 2018. 236: p. 44-53.

15. Alenad, A.M., et al., Polyaniline-engineered zinc sulphidenanocomposite as a highly efficient electrocatalyst for the oxygen evolution process. Journal of the Korean Ceramic Society, 2023: p. 1-13.
16. Chitra, P., et al., Effect of ultrasonication on particle size and magnetic properties of polyaniline NiCoFe2O4 nanocomposites. Journal of magnetism and magnetic materials, 2014. 366: p. 55-63.
17. Shahabuddin, S., et al., Synthesis and characterization of Co 3 O 4 nanocube-doped polyanilinenanocomposites with enhanced methyl orange adsorption from aqueous solution. RSC advances, 2016. 6(49): p. 43388-43400.
18. Ghahremanloo, A., et al., Electroconductive and photoactive poly (phenylenediamine) s with antioxidant and antimicrobial activities for potential photothermal therapy. New Journal of Chemistry, 2022. 46(13): p. 6255-6266.
19. Kheyrabadi, F.B. and E.N. Zare, Antimicrobial nanocomposite adsorbent based on poly (meta-phenylenediamine) for remediation of lead (II) from water medium. Scientific Reports, 2022. 12(1): p. 4632.
20. Alenad, A.M., et al., Highly performed tungsten trioxide-polyaniline composite thin film and their accelerated oxygen evolution electrocatalyst activity. Journal of Electroanalytical Chemistry, 2023. 941: p. 117550.
21. Taha, T. and K.S. El-Nasser, Synthesis, thermal and dielectric investigations of PVDF/PVP/Co 0.6 Zn 0.4 Fe 2 O 4 polymer nanocomposite films. Journal of Materials Science: Materials in Electronics, 2021. 32: p. 27339-27347.
22. Alshammari, A.H. and T. Taha, Structure, thermal and dielectric insights of PVC/PVP/ZnFe2O4 polymer nanocomposites. The European Physical Journal Plus, 2021. 136(12): p. 1201.
23. Taha, T., et al., Micro-structure, thermal, and dielectric performance of polyester nanocomposites containing nano-Ni 0.5 Zn 0.5 Fe 2 O 4. Applied Physics A, 2020. 126: p. 1-10.
24. Kumar, K.S., et al., Synthesis, magnetic and dielectric properties of poly (m-phenylenediamine)/ZnNiFe2O4 nanocomposites. Inorganic Chemistry Communications, 2024. 161: p. 111983.
25. Maged, F.A., et al., Comparative study of CdS&TiO2 based polyaniline/polyvinyl alcohol nanocomposites as electrode for supercapacitors. PhysicaScripta, 2022. 97(11): p. 115805.
26. Moussa, M.A., et al., Dielectric investigations and charge transport in PS-PAni composites with ionic and nonionic surfactants. Journal of Physics and Chemistry of Solids, 2019. 133: p. 163-170.
27. Abomostafa, H., et al., Investigation of structure, thermal and dielectric study of Dy0. 05Ba0. 7Sr0. 25TiO3/polystyrene nanocomposites.PhysicaScripta, 2023. 98(8): p. 085919.
28. Kremer, F. and A. Schönhals, Broadband dielectric spectroscopy. 2002: Springer Science & Business Media.
29. Tohamy, H.-A.S., et al., Antibacterial activity and dielectric properties of the PVA/cellulose nanocrystal composite using the synergistic effect of rGO@ CuNPs. International Journal of Biological Macromolecules, 2024: p. 129801.
30. Khairy, M. and M.E. Gouda, Electrical and optical properties of nickel ferrite/polyanilinenanocomposite. J Adv Res, 2015. 6(4): p. 555-62.
31. Yan, J., et al., Preparation of a graphenenanosheet/polyaniline composite with high specific capacitance. Carbon, 2010. 48(2): p. 487-493.
32. Henaish, A.M.A., et al., Synthesis, Electric and Magnetic Characterization of Nickel Ferrite/PANI Nano-Composite Prepared by Flash Auto Combustion Method. Journal of Inorganic and Organometallic Polymers and Materials, 2020. 31(2): p. 731-740.
33. Sehrawat, S., et al., A Comparative Analysis of Structural, Optical and Electrical Properties of Polyaniline/Ferrite (Co, Ni, Cu, Zn) Composites. ECS Journal of Solid State Science and Technology, 2022. 11(11): p. 113005.
34. Jambaladinni, S. and J.S. Bhat, The Role of ZnONanofillers in Enhancing the Properties of PVA/PVP Blend Nanocomposites. Iranian Journal of Science and Technology, Transactions A: Science, 2021. 45(5): p. 1851-1860.
35. Rithin Kumar, N.B., V. Crasta, and B.M. Praveen, Dielectric and electric conductivity studies of PVA (Mowiol 10-98) doped with MWCNTs and WO3nanocomposites films. Materials Research Express, 2016. 3(5): p. 055012.
36. Kumar, N.B.R., V. Crasta, and B.M. Praveen, Advancement in Microstructural, Optical, and Mechanical Properties of PVA (Mowiol 10-98) Doped by ZnO Nanoparticles. Physics Research International, 2014. 2014: p. 1-9.
37. Abdullah, A.M., S.B. Aziz, and S.R. Saeed, Structural and electrical properties of polyvinyl alcohol (PVA):Methyl cellulose (MC) based solid polymer blend electrolytes inserted with sodium iodide (NaI) salt. Arabian Journal of Chemistry, 2021. 14(11): p. 103388.
38. Somesh, T.E., et al., Photosensitization of optical band gap modified polyvinyl alcohol films with hybrid AgAlO2 nanoparticles. Journal of Materials Science: Materials in Electronics, 2018. 30(1): p. 37-49.
39. López, R. and R. Gómez, Band-gap energy estimation from diffuse reflectance measurements on sol–gel and commercial TiO2: a comparative study. Journal of Sol-Gel Science and Technology, 2011. 61(1): p. 1-7.
40. Yesappa, L., et al., Characterization, Electrical Conductivity and Electrochemical Performance of Polyaniline-LiClO4-CuO Nano Composite for Energy Storage Applications. Polymer-Plastics Technology and Materials, 2018. 58(2): p. 193-205.
41. Andreas, R., A. Lesbani, and F. Akhmad Yusuf, The character istics (compositions, morphological, and structure) of nanocompositespolyaniline (PANI)/ZnO. IOP Conference Series: Materials Science and Engineering, 2019. 509: p. 012126.
42. Xia, Y., J.M. Wiesinger, and A.G. MacDiarmid, Camphorsulfonic Acid Fully Doped PolyanilineEmeraldine Salt: Conformations in Different Solvents Studied by an UltravioletNisiblel Near-Infrared Spectroscopic Method. Chem. Mater., 1995. 7: p. 443-445.
43. Abdiryim, T., Z. Xiao-Gang, and R. Jamal, Comparative studies of solid-state synthesized polyaniline doped with inorganic acids. Materials Chemistry and Physics, 2005. 90(2-3): p. 367-372.
44. Abd El-Ghany, W.A., N.H.S. Nasralla, and G.M. El Komy, Structure and optical properties of spray deposited Cu–Mn–O thin films for optoelectronic devices. Optical Materials, 2022. 127: p. 112319.
45. Aamir, M., et al., Synthesis and characterizations of Co–Zr doped Ni ferrite/PANI nanocomposites for photocatalytic methyl orange dye degradation. Physica B: Condensed Matter, 2022. 624: p. 413392.

46. Zhang, X., et al., NiCo alloy/C nanocomposites derived from a Ni-doped ZIF-67 for lightweight microwave absorbers. Nanotechnology, 2021. 32(38): p. 385602.
47. Khairy, M., Synthesis, characterization, magnetic and electrical properties of polyaniline/NiFe2O4 nanocomposite. Synthetic metals, 2014. 189: p. 34-41.
48. Yang, H., et al., Synthesis and microwave absorbing properties of polyaniline/CoFe2O4/Ba0.4Sr0.6TiO3 composites. Journal of Materials Science: Materials in Electronics, 2016. 27(10): p. 10849-10854.
49. Cullity, B.D. and C.D. Graham, Introduction to magnetic materials. 2011: John Wiley & Sons.
50. Atef, N., et al., Dielectric Studies on CuO-Na 2 OB 2 O 3 Glasses. New Journal of Glass and Ceramics, 2020. 10(04): p. 45.
51. Maxwell, J.C., A treatise on electricity and magnetism. Vol. 1. 1873: Clarendon press.
52. Rezlescue, N. and E. Rezlescu, Study of structural and magnetic properties of Ni-Mg ferrites. J. Phys. Status Solidi A, 1974. 23: p. 575.
53. Chakradhary, V.K. and M.J. Akhtar, Absorption properties of CNF mixed cobalt nickel ferrite nanocomposite for radar and stealth applications. Journal of Magnetism and Magnetic Materials, 2021. 525: p. 167592.
54. Hussain, H.V., et al., Polymer based nickel ferrite as dielectric composite for energy storage applications. Synthetic Metals, 2020. 268: p. 116507.